SPITZER INFRARED SPECTROGRAPH DETECTION OF MOLECULAR HYDROGEN ROTATIONAL EMISSION TOWARDS TRANSLUCENT CLOUDS

James G. Ingalls[1], T. M. Bania[2], F. Boulanger[3], B. T. Draine[4], E. Falgarone[5], and P. Hily-Blant[6]

[1] Spitzer Space Telescope Science Center, California Institute of Technology, 1200 E California Blvd, Mail Stop 220-6, Pasadena, CA 91125, USA; ingalls@ipac.caltech.edu
[2] Institute for Astrophysical Research, Boston University, 725 Commonwealth Avenue, Boston, MA 02215, USA; bania@bu.edu
[3] Institut d'Astrophysique Spatiale, Université Paris Sud, Bat. 121, F-91405 Orsay Cedex, France; francois.boulanger@ias.u-psud.fr
[4] Princeton University Observatory, Peyton Hall, Princeton, NJ 08544, USA; draine@astro.princeton.edu
[5] Laboratoire de Radio-Astronomie, LERMA, Ecole Normale Supérieure, 24 rue Lhomond, F-75231 Paris Cedex 05, France; edith.falgarone@lra.ens.fr
[6] LAOG, CNRS UMR 5571, Université Joseph Fourier, BP53, F-38041 Grenoble, France; pierre.hilyblant@obs.ujf-grenoble.fr

ABSTRACT

Using the Infrared Spectrograph on board the *Spitzer Space Telescope*, we have detected emission in the S(0), S(1), and S(2) pure-rotational ($v = 0–0$) transitions of molecular hydrogen (H_2) toward six positions in two translucent high Galactic latitude clouds, DCld $300.2-16.9$ and LDN 1780. The detection of these lines raises important questions regarding the physical conditions inside low-extinction clouds that are far from ultraviolet radiation sources. The ratio between the S(2) flux and the flux from polycyclic aromatic hydrocarbons (PAHs) at 7.9 μm averages 0.007 for these six positions. This is a factor of about four higher than the same ratio measured toward the central regions of non-active Galaxies in the *Spitzer* Infrared Nearby Galaxies Survey. Thus, the environment of these translucent clouds is more efficient at producing rotationally excited H_2 per PAH-exciting photon than the disks of entire galaxies. Excitation analysis finds that the S(1) and S(2) emitting regions are warm ($T \gtrsim 300$ K), but comprise no more than 2% of the gas mass. We find that UV photons cannot be the sole source of excitation in these regions and suggest mechanical heating via shocks or turbulent dissipation as the dominant cause of the emission. The clouds are located on the outskirts of the Scorpius-Centaurus OB association and may be dissipating recent bursts of mechanical energy input from supernova explosions. We suggest that pockets of warm gas in diffuse or translucent clouds, integrated over the disks of galaxies, may represent a major source of all non-active galaxy H_2 emission.

Key words: infrared: ISM – ISM: individual objects (DCld 300.2-16.9, MBM 33, LDN 1780) – ISM: lines and bands – ISM: molecules

1. INTRODUCTION

The kinetic temperature of all cold ($T < 100$ K) diffuse interstellar clouds is the result of a balance between heating and cooling processes. The H I and H_2 receive kinetic energy from electrons ejected from dust grains and polycyclic aromatic hydrocarbons (PAHs) by interstellar far-ultraviolet (FUV; 6 eV$< h\nu <$ 13.6 eV) photons, and transfer that energy to all other gas phase constituents. Clouds are cooled when inelastic collisions lead to spontaneous emission of spectral line radiation. Despite its being the most abundant constituent of molecular clouds, the role of H_2 in directly cooling the diffuse interstellar medium (ISM) via its own line emission is uncertain. Spitzer (1949) was the first to estimate the significance of the pure-rotational ($v = 0–0$) transitions of H_2 in cooling interstellar matter. Since that time, it has been realized that other species (C II in atomic gas and CO in UV-shielded molecular gas) were much more efficient at converting kinetic energy to line emission, despite their much lower abundances ($\sim10^{-4}$) relative to hydrogen (Wolfire et al. 2003; Hollenbach et al. 1991).

Because of the small moment of inertia of H_2, its rotational energy levels are difficult to excite in the cold ISM. The lowest-lying transitions are the electric quadrupole pure-rotational lines. Because H_2 lacks an electric dipole moment, the $J = 1$ level is unable to radiate, so the first radiating level is $J = 2$. The first three rotational transitions are thus S(0) ($J = 2–0$) at 28.2 μm, S(1) ($J = 3–1$) at 17.0 μm, and S(2) ($J = 4–2$) at 12.3 μm. All were observable with the *Spitzer* Infrared Spectrograph (IRS). The lowest transition S(0) has

$h\nu/k = 510$ K. The S(2) transition occurs from a rotational level ($J = 4$) that is about 1700 K above the ground state.

Knowledge of the distribution of physical conditions along a given line of sight is required for the proper interpretation of any observation of H_2 lines. This is especially true for path lengths spanning many kpc such as the disks of galaxies. Since these quadrupole transitions require high temperatures to excite by collisions, the presence of H_2 lines in the ISM of galaxies is usually thought to be the result of either collisional excitation in warm H_2 or UV pumping. Collisional excitation is expected to dominate in shock waves, while UV pumping dominates the excitation in photodissociation regions (PDRs; e.g., Shull & Hollenbach 1978; Bertoldi et al. 2000; Meyer et al. 2001). In other cases, however, the source of H_2 excitation is not so clear. In the recent *Spitzer* Infrared Nearby Galaxies Survey (SINGS; Kennicutt et al. 2003) measurements of H_2 in normal galaxies, Roussel et al. (2007) concluded that FUV-rich PDRs at the interfaces between bright H II regions and molecular clouds were the most likely source of the emission. The authors did note that some of the H_2 flux could originate in diffuse gas illuminated by the ambient FUV field ($G_0 \sim 1$, in units of the average interstellar radiation field (ISRF) near the Sun), which is in fact the source of most of the IR emission in the same sample (Draine et al. 2007). But their paper did not favor this interpretation of their data.

A growing body of analysis finds that the H_2 emission from the disks of galaxies *does* originate partly in diffuse material. Using *Far-Ultraviolet Spectroscopic Explorer* (*FUSE*) measurements of FUV absorption by H_2 toward late B stars

Table 1
Observed H_2 and Dust Surface Brightness

| Position | R.A. (2000) (hh:mm:ss.s) | Decl. (2000) (dd:mm:ss) | H_2 Pure-rotational Surface Brightness[a] | | | | | | | $I_{7.9,PAH}$[b] (10^{-7}) | TIR[c] (10^{-6}) |
| | | | S(0) | S(1) | S(2) | S(3) | S(4) | S(5) | S(6) | | |
						$(10^{-10}\,W\,m^{-2}\,sr^{-1})$					
DCld 300.2-16.9 (C)	11:48:24.4	−79:18:00	36.74 ±0.16	13.5 ±0.4	12.8 ±0.5	<4.0[d]	<6.8	<4.7	<8.0	2.436 ±0.007	1.64 ±0.16
DCld 300.2-16.9 (B)	11:52:08.3	−79:09:33	29.43 ±0.16	13.5 ±0.4	8.9 ±0.4	<3.8	<5.8	<5.3	<11.2	2.745 ±0.015	3.4 ±0.3
DCld 300.2-16.9 (A)	11:54:23.1	−79:31:42	24.03 ±0.15	9.4 ±0.4	7.7 ±0.5	<3.4	<4.0	<4.3	<5.4	2.137 ±0.018	1.51 ±0.15
DCld 300.2-16.9 (D)	11:55:33.8	−79:20:54	26.27 ±0.14	9.7 ±0.4	9.0 ±0.5	<4.2	<5.1	<5.0	<5.4	1.714 ±0.005	0.83 ± 0.08
LDN 1780 (7)	15:39:23.0	−07:10:05	...	...	6.9 ±0.6	<5.4	<3.2	<1.5	<3.2	0.742 ±0.003	1.47 ±0.14
LDN 1780 (3)	15:40:34.2	−07:13:14	...	...	20.9 ±0.6	<4.6	<5.4	<9.5	<7.6	1.533 ±0.002	2.7 ±0.3

Notes.
[a] Integrated H_2 surface brightness from spectrum fits, in units of $10^{-10}\,W\,m^{-2}\,sr^{-1}$.
[b] $I_{7.9,PAH} \equiv \langle \nu I_\nu \rangle_{7.9\mu m}$ measured over the *Spitzer* IRAC 7.9 μm band. Units are $10^{-7}\,W\,m^{-2}\,sr^{-1}$.
[c] Estimated total infrared surface brightness, in units of $10^{-6}\,W\,m^{-2}\,sr^{-1}$.
[d] Upper limits are 3σ, as described in the text.

behind the Chamaeleon complex, Gry et al. (2002) found that the rotational levels could not be populated by only FUV photons, and required collisional excitation within anomalously warm regions. Indeed, further study of the cirrus cloud in front of these stars (Nehmé et al. 2008a) has determined that the observed CH$^+$ absorption also depends on the existence of warm pockets of gas, since the formation of CH$^+$ molecules needs an activation energy of $\Delta E/k = 4640$ K. The first detection of pure-rotational H_2 emission from diffuse Galactic regions was the Falgarone et al. (2005) *Infrared Space Observatory* (*ISO*) SWS measurement of the S(0) to S(3) transitions along a direction in the mid-plane of the Milky Way (MW: $l, b = 26°46, 0°09$). As concluded from the absorption result of Gry et al. (2002), the MW H_2 emission turns out to be *too bright* to be caused only by FUV excitation.

In this paper, we give additional evidence that low-extinction, low-UV environments can excite H_2 molecules. In the following section, we describe recent ultra-sensitive *Spitzer Space Telescope* observations of the 5–15 μm (5–38 μm for four positions) spectrum toward translucent clouds at high Galactic latitude ($|b| \gtrsim 15$ deg) associated with infrared cirrus. In Section 3, we show detections of H_2 S(0) and S(1) emission toward four positions and S(2) emission toward six positions. We estimate the physical conditions in the regions producing H_2 line radiation. We compute ratios of H_2 flux to PAH feature strength and compare with the measurements of the same quantities made as part of the *Spitzer* Legacy SINGS survey of non-active galaxies. In Section 4, we review possible sources of excitation of the H_2 molecules, and discuss the implications for the study of H_2 emission from the disks of galaxies. In Section 5, we make our concluding remarks.

2. OBSERVATIONS

2.1. Spitzer Spectroscopic Measurements

As part of a study of the heating and cooling of high Galactic latitude translucent clouds (HLCs), we spectrally imaged 34 positions in six HLCs at 5.2–14.5 μm using *Spitzer* (Werner et al. 2004) IRS (Houck et al. 2004). The data were taken under General Observer programs 20093 and 40207. We detected six

positions in two of the clouds, DCld 300.2–16.9 and LDN 1780 ($l, b \approx 358°9, +36°9$), in H_2 S(2) pure-rotational emission at 12.3 μm. The data for position A of cloud DCld 300.2–16.9 (*Spitzer* Request Key [SRK] 0014030848) were obtained on 2005 July 9; those for positions B, C, and D (SRK 0022715136) were obtained on 2007 July 24; and those for LDN 1780 positions 3 (SRK 0022715648) and 7 (SRK 0022715392) were obtained on 2008 March 26. In addition, we imaged the 14–38 μm spectrum toward four positions in DCld 300.2–16.9 under Director's Discretionary Time program 491. These measurements (SRK 0028315392) were obtained on 2009 April 16 and yielded H_2 S(0) 28.2 μm and S(1) 17.0 μm detections toward all positions. The coordinates of the H_2-detected positions are given in Table 1. Those for the undetected positions are provided in Table 2. Although we present some of the dust measurements in this paper, a full analysis of the interstellar dust emission in the six-cloud sample is the subject of a future paper (J. G. Ingalls et al. 2011, in preparation). We describe in this section the method by which we measured the S(0), S(1), and S(2) emission.

Figure 1 shows the orientations and areas of coverage of the IRS subslits that we used to produce spectra for the four positions in DCld 300.2–16.9 and the two positions in LDN 1780. The slit apertures are shown superimposed on 100 μm emission maps from the *IRAS* Sky Survey Atlas (ISSA). The 5.2–14.5 μm measurements of both clouds were made using the IRS short-wavelength low-resolution (SL) module. Each target was observed in standard staring mode for eight cycles of 60 s each. Under staring mode, for each data collection cycle the SL2 subslit (5.2–7.7 μm), and then the SL1 subslit (7.4–14.5 μm), are each placed on the target position at two offset "nod" positions, 1/3 and 2/3 along the long axis of the $57'' \times 3''.7$ subslit. When one subslit observed the target, the other subslit observed a region of adjacent sky. The two subslits are separated by $22''$. (For a complete description of the SL geometry, see the IRS Instrument Handbook (SSC 2009).) We spent a total of about 32 minutes imaging a $234'' \times 3''.7$ region around each target. Since each subslit observes a different region of adjacent sky, the area of overlap between the two subslits was

<div align="center">

Table 2
Positions with H_2 Upper Limits and Dust Surface Brightness

</div>

Position	R.A. (2000) (hh:mm:ss.s)	Decl. (2000) (dd:mm:ss)	S(2)	S(3)	S(4)	S(5)	S(6)	$I_{7.9,\mathrm{PAH}}$[b] (10^{-7})
			H2 Pure-rotational Upper Limits[a] (10^{-10} W m^{-2} sr^{-1})					
MBM 12 (01)	02:56:09.6	+19:26:51	39.3	60.7	90.4	54.7	85.6	1.264 ± 0.018
MBM 12 (A; −509.1,+636.4)[c]	02:56:19.9	+19:26:04	2.6	4.1	2.6	8.4	3.7	0.573 ± 0.007
MBM 12 (A; −381.8,+509.1)	″	″	2.2	4.7	2.5	8.5	5.8	0.681 ± 0.022
MBM 12 (A; −254.6,+381.8)	″	″	11.6	40.2	28.2	15.6	23.7	1.09 ± 0.03
MBM 12 (A; −254.6,+381.8)	″	″	11.6	40.2	28.2	15.6	23.7	1.09 ± 0.03
MBM 12 (A; −127.3,+254.6)	″	″	15.6	78.0	35.7	23.6	33.7	0.88 ± 0.05
MBM 12 (A; 0,+127.3)	″	″	12.4	52.6	24.9	24.6	23.6	0.62 ± 0.03
MBM 12 (A; +127.3,-254.6)	″	″	14.0	102.0	32.3	22.8	28.8	0.78 ± 0.24
MBM 12 (A; +254.6,-381.8)	″	″	9.0	26.8	17.5	16.2	18.6	0.962 ± 0.022
MBM 12 (A; +381.8,-509.1)	″	″	2.9	4.1	3.8	7.0	3.6	0.634 ± 0.015
MBM 12 (A; +509.1,-636.4)	″	″	2.5	5.4	2.7	9.7	4.9	0.570 ± 0.006
MBM 12 (10)	02:56:40.4	+19:24:20	24.2	87.3	72.4	41.9	57.6	1.15 ± 0.03
MBM 12 (01 off)	02:57:07.9	+19:16:17	14.8	38.2	38.0	22.0	29.9	1.039 ± 0.022
MBM 12 (12)	02:57:27.2	+20:02:45	33.7	51.3	79.9	56.8	61.7	1.866 ± 0.019
MBM 12 (12 off)	02:58:39.0	+20:14:16	45.0	69.4	106.7	62.5	85.0	1.472 ± 0.017
MBM 28 (A)[d]	09:29:09.2	+70:31:00	35.5	55.0	...	...	...	...
DCld 300.2-16.9 (E)	11:46:18.9	−78:46:33	1.3	2.5	3.1	7.2	5.6	0.562 ± 0.011
LDN 183 (W1; −540,0)	15:52:54.5	−02:52:24	2.7	7.9	6.7	6.1	7.6	1.341 ± 0.018
LDN 183 (W1; −360,0)	″	″	2.9	6.6	6.9	3.8	4.7	1.527 ± 0.015
LDN 183 (W1; −180,0)	″	″	3.8	9.2	10.0	6.6	7.6	1.675 ± 0.017
LDN 183 (W1; 0,0)	″	″	3.2	9.2	11.2	6.5	5.0	1.329 ± 0.013
LDN 183 (W1; +180,0)	″	″	2.7	4.0	7.3	13.9	13.2	1.033 ± 0.009
LDN 183 (W1; +360,0)	″	″	2.7	4.8	6.9	12.9	13.2	0.960 ± 0.018
LDN 183 (W1; +540,0)	″	″	2.8	5.0	6.7	13.3	14.3	0.902 ± 0.009
Stark 4 (S1; −480,0)	23:45:07.3	−71:42:47	5.2	9.1	13.7	12.3	16.2	<0.340[e]
Stark 4 (S1; −240,0)	″	″	3.3	5.4	7.4	6.1	8.4	0.113 ± 0.016
Stark 4 (S1; 0,0)	″	″	2.1	3.4	5.3	5.2	6.4	0.206 ± 0.019
Stark 4 (S1; +240,0)	″	″	3.4	4.7	8.0	5.3	5.3	0.178 ± 0.006
Stark 4 (S1; +480,0)	″	″	7.7	10.4	15.5	11.1	14.0	0.299 ± 0.012

Notes.
[a] Integrated H_2 surface brightness upper limits (3σ) from spectrum fits, in units of 10^{-10} W m^{-2} sr^{-1}.
[b] $I_{7.9,\mathrm{PAH}} \equiv \langle \nu I_\nu \rangle_{7.9\mu m}$ measured over the *Spitzer* IRAC 7.9μm band. Units are 10^{-7} W m^{-2} sr^{-1}.
[c] Offset from AOR center given as (ΔR.A., Δdecl.), in arcseconds.
[d] The SL2 portion of the spectrum for MBM 28 (A) was corrupted by stray light and did not yield measurements for S(3) through S(6), nor for $I_{7.9,\mathrm{PAH}}$.
[e] Upper limit to $I_{7.9,\mathrm{PAH}}$ is three times the rms in the band.

only $95'' \times 3''.7$. Nevertheless in what follows we combine all observations in the $234''$ window covered by either SL1 or SL2 (yellow in Figure 1). The results do not change if we limited the measurements to within the $95''$ region of overlap, although the noise increases noticeably.

The 14–38 μm measurements toward four positions in DCld 300.2–16.9 were made using the IRS long-wavelength low-resolution (LL) module, whose slit covers a larger region of the sky than SL. Each of the four targets (plus the background position—see below) was observed in staring mode for 24 cycles of 30 s each. As for the SL observations, the short (LL1 subslit; 14.0–21.3 μm) and long (LL2 subslit; 19.5–38.0 μm) wavelength portions of the spectra were imaged on different portions of the sky. In the case of LL, however, we only combined the data for the two subslit positions that overlapped on the sky, yielding about 24 minutes per position and covering a $280'' \times 10''.6$ region (red in Figure 1(a)). To increase the likelihood of scheduling these measurements, we did not constrain the observation dates, and therefore the SL slit position angles were not replicated exactly by the LL measurements. This resulted in SL and LL effective apertures that were well matched in size, but only overlapped a relatively small portion of sky, near the centers

of the imaged regions (see Figure 1). In other words, we have chosen to minimize random noise (maximize integration time per area of sky) at the expense of systematic error due to mismatched position angle, assuming that the emission is not a strong function of position.

Our clouds all lie in regions of relatively bright Zodiacal emission (according to the *Spitzer* Planning Observations Tool (SPOT)[7] background estimator, the Zodiacal foreground at 7.7 μm ranges from 5 to 15 MJy sr^{-1}). To measure this sky foreground as well as correct for short-term detector drifts, every observation (or concurrent group of observations) of a given cloud was accompanied by an off-source "background" measurement with the same integration parameters. The background position was taken to be a local minimum in a $5° \times 5°$ ISSA 100 μm map centered on the cloud. The following sky background positions were observed (equatorial J2000): DCld 300.2–16.9 (11:41:33.7,−78:11:37); LDN 1780 (15:33:50.9,−07:28:26); MBM 12 (02:51:36.0,+19:10:03); MBM 28 (09:38:34.9,+71:13:58); LDN 183 (15:48:48.8, −00:34:35); and Stark 4 (23:52:41.1,−71:12:45).

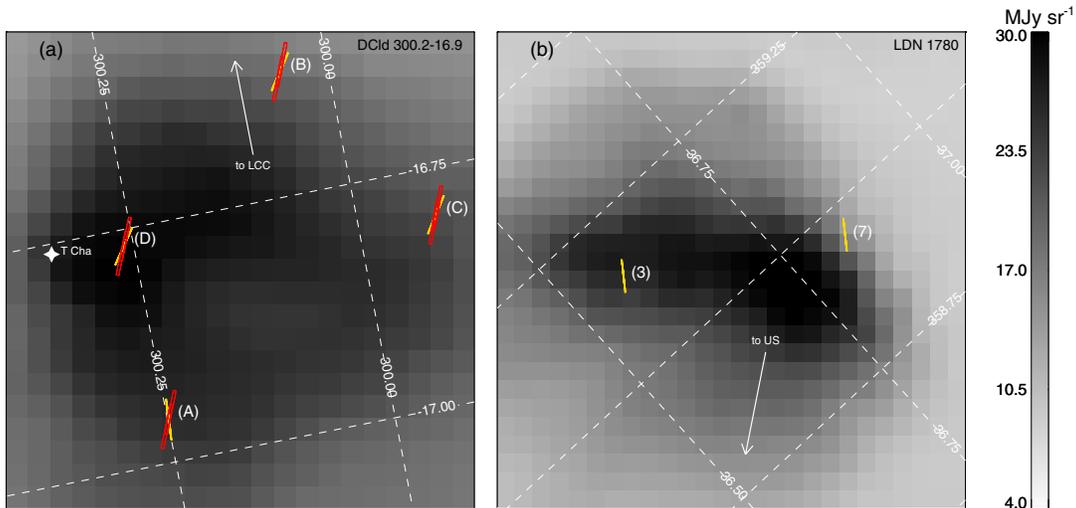**Figure 1.** *IRAS* Sky Survey Atlas images of the 100 μm emission toward (a) DCld 300.2–16.9 and (b) LDN 1780. Superposed are images of the SL (yellow) and LL (red) slit apertures used for our measurements. The direction toward the Lower Centaurus Crux and Upper Scorpius OB associations are shown by arrows on the left and right panels, respectively. In these images, celestial north is up and Galactic coordinates are indicated by a dashed grid.

2.2. Data Reduction

Data processing started with the basic calibrated data (`bcd.fits`) spectral image files from the S18.7 *Spitzer* IRS calibration pipeline. As mentioned above, to maximize the signal-to-noise ratio in the SL data, we combined all 32 spectral images toward a given position, covering a $234'' \times 3\rlap{.}''7$ region on the sky. We used an outlier-resistant computation of the mean (`resistant_mean.pro` from the IDL Astronomy User's Library[8]) of the 32 measurements for each pixel. For the LL data, we combined similarly the 48 spectral images covering the inner $280'' \times 10\rlap{.}''6$ region covered by both subslits. To remove Zodiacal foreground emission and residual dark current, and to minimize the effects of "rogue" pixels that vary on timescales greater than a few hours, we subtracted a mean image of the nearby sky (see above) from each mean source image. We used IRSCLEAN[9] to interpolate over any remaining rogue pixels in each of the sky-subtracted mean images. We extracted full slit extended source calibrated spectra from the resulting images using the *Spitzer* IRS Custom Extraction tool (SPICE).[10]

We combined the surface brightness spectra for SL orders 1 and 2 into a single spectrum covering the wavelength range 5.79–14 μm. To do this we re-gridded the $\Delta\lambda = 0.04\,\mu$m SL2 spectrum to match the 0.06 μm SL1 wavelength grid using linear interpolation, and averaged SL1 and SL2 values where the two orders covered the same wavelengths. Before combining, the edge of each order was trimmed by from 2–15 spectral elements to eliminate regions of poor responsivity. This process was repeated for the LL data, giving a combined LL spectrum with a resolution of 0.17 μm covering the wavelength range 14.2–35.8 μm. To obtain a 5.79–35.8 μm spectrum for the four positions with LL measurements, the SL and LL spectra for these four positions were concatenated together, retaining the different resolutions. We used the PAHFIT package (Smith et al. 2007) to fit simultaneously a set of PAH dust features, gas phase lines (including the H_2 pure-rotational lines), dust continuum emission, and an extinction curve. The fits were weighted by

the error spectrum produced by the *Spitzer* IRS pipeline and SPICE. Uncertainties for all fit parameters were computed by PAHFIT using full covariance matrices for the multicomponent fits. A proper fit to the data required modification of the default PAHFIT parameters. The 12.69 μm PAH feature seems to be considerably wider in these spectra than expected from PAHFIT default parameters, resulting in spurious detections of the [Ne II] 12.8 μm line when the default narrow 12.69 μm width was used. This left a "knee" of emission in the model spectrum that was not visible in the data. We found that increasing the fractional FWHM of the 12.69 μm Drude profile, from $\gamma_r(12.69) = 0.013$ to 0.042 (the same as for the 12.62 μm feature), removed the spurious knee and eliminated the [Ne II] "detection."

For the S(3) through S(6) H_2 lines, which were not detected, we estimated 3σ upper limits to the integrated intensity as follows. First, we subtracted the fit to all PAH features and dust continuum components from the observed spectrum. We divided the result by the PAHFIT-derived extinction curve (which in most cases did not affect the S(2) or 7.9 μm intensities by more than 10%). For a given H_2 line we then determined $\sigma_{\rm rms}$, the root mean square of this residual extinction-corrected spectrum in a wavelength region centered on the line center wavelength, $\lambda_0 \pm 4 \times {\rm FWHM}_\lambda$. Since all molecular lines are unresolved by the IRS, the expected full width at half maximum (${\rm FWHM}_\lambda$) of the line is determined only by instrumental parameters (see Smith et al. 2007, for more details on the H_2 line parameters). For a Gaussian line profile with peak intensity $I_{\lambda,{\rm peak}}$ the integrated intensity is given by

$$I \equiv \int I_\lambda d\lambda = \frac{\sqrt{2\pi}\,({\rm FWHM}_\lambda)}{2\sqrt{2\ln 2}} I_{\lambda,{\rm peak}}$$
$$\approx 1.064\,({\rm FWHM}_\lambda)\, I_{\lambda,{\rm peak}}. \qquad (1)$$

Thus, the 3σ integrated surface brightness limit is determined by substituting $3\sigma_{\rm rms}$ for $I_{\lambda,{\rm peak}}$ in Equation (1):

$$\frac{I}{{\rm W\,m^{-2}\,sr^{-1}}} < 3.191 \times 10^{-6} \left(\frac{\lambda_0}{\mu{\rm m}}\right)^{-2} \left(\frac{{\rm FWHM}_\lambda}{\mu{\rm m}}\right)$$
$$\times \left(\frac{3\,\sigma_{\rm rms}}{{\rm MJy\,sr^{-1}}}\right). \qquad (2)$$
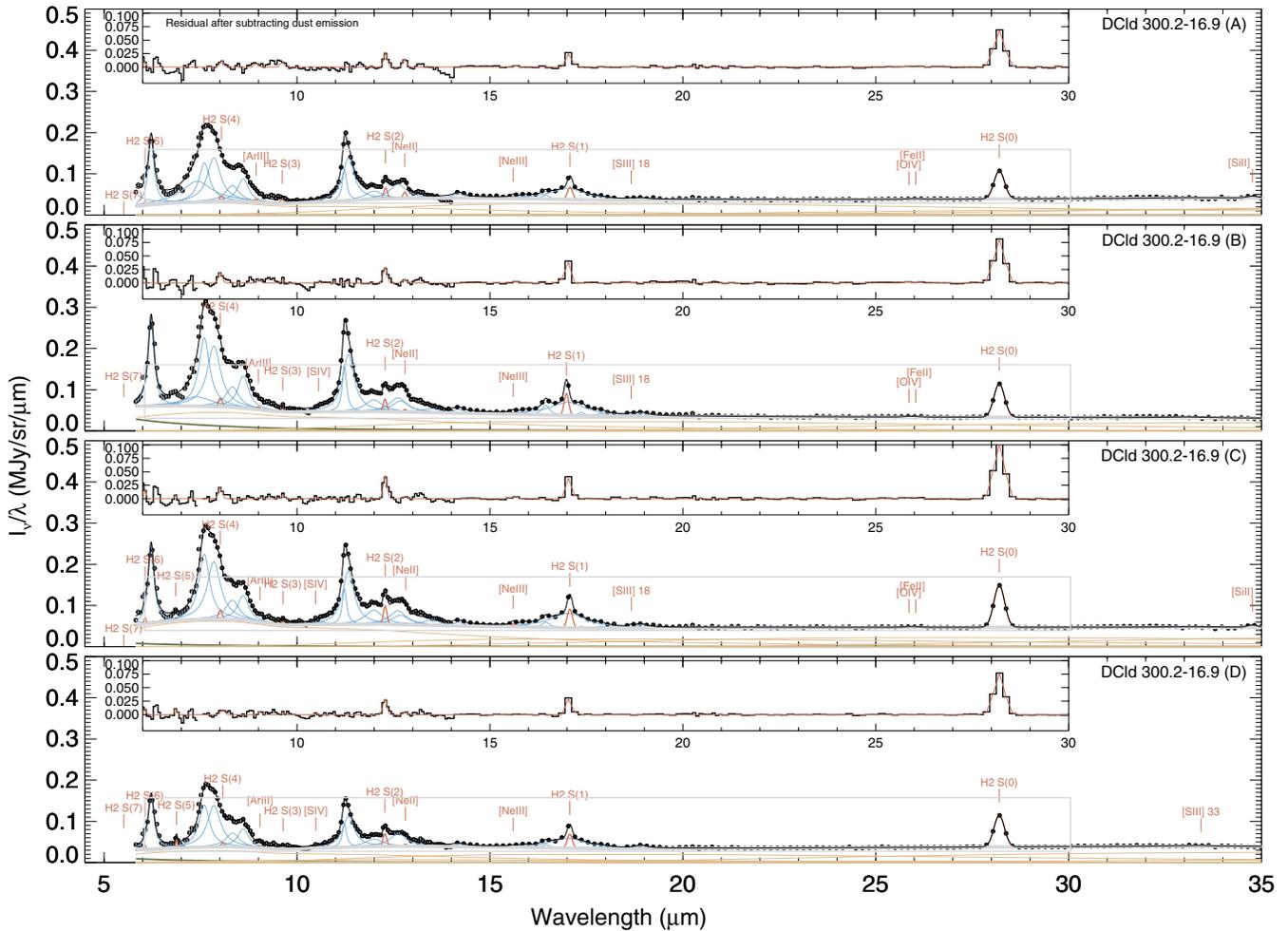
Figure 2. *Spitzer* IRS observed spectra (filled circles with error bars) for four positions in DCld 300.2–16.9 in front of the Chamaeleon complex. Superimposed on the spectra are fits (solid black line) made using the PAHFIT program (Smith et al. 2007), that are each the sum of three dust continuum components (brown), a 5000 K stellar blackbody (green), gas phase spectral lines (red), and a set of PAH features (blue), and account for silicate extinction. The thick gray curves indicate the total continuum emission. The inset figures show the residuals in the data for a portion of the spectrum (solid histogram), after subtracting off the fits to the dust continuum and PAH features and correcting for extinction. The summed fits to all gas phase spectral lines are superimposed in red on the inset plots. All inset plot windows cover the same range in wavelength as the region of the main plot window they occupy. The size of each inset window in its main plot window is given by a gray rectangle overlaid on the full spectrum.

2.3. Dust Emission

To constrain the amount of interstellar radiation processed by cirrus clouds, we synthesized broadband measurements of the dust emission. For all positions, we computed $I_{7.9,\mathrm{PAH}} = \langle \nu I_\nu \rangle_{7.9,\mathrm{PAH}}$, the PAH surface brightness in *Spitzer* Infrared Array Camera (IRAC) band 4, which is centered on 7.9 μm. To do this we integrated the model PAH spectrum (given by the sum of fits to PAH features in Figures 2 and 3) weighted by the IRAC 4 filter response, and multiplied the result by the color correction (SSC 2010a) to give the specific intensity ($\mathrm{MJy\,sr}^{-1}$) that would be measured photometrically on an IRAC image. Multiplying by the effective frequency of the 7.9 μm array gives the surface brightness ($\mathrm{W\,m}^{-2}\,\mathrm{sr}^{-1}$). This procedure was implemented using the *Spitzer* Synthetic Photometry software.[11] Error bars for $I_{7.9,\mathrm{PAH}}$ are derived from the covariance matrix for the fit PAH parameters. For the position in Table 2 that did not have detectable PAH features we computed upper limits as three times the rms spectrum integrated over IRAC band 4 (the spectrum was squared, integrated over the band, and multiplied

by the color correction; the square root of this was multiplied by the effective frequency).

We made a crude estimate of the total infrared (TIR) surface brightness to compare with the total H_2 emission from the S(0) to S(2) transitions. We converted the formula given in Equation (22) of Draine & Li (2007) from spectral luminosity to surface brightness:

$$\mathrm{TIR} \approx 0.95 \langle \nu I_\nu \rangle_{7.9} + 1.15 \langle \nu I_\nu \rangle_{24} + \langle \nu I_\nu \rangle_{71} + \langle \nu I_\nu \rangle_{160}. \quad (3)$$

The ν values are the effective frequencies (in Hz) of the *Spitzer* IRAC 7.9 and MIPS 24, 71, and 160 μm bandpasses, and I_ν is the specific intensity measured with these instruments.

The surface brightness $\langle \nu I_\nu \rangle_{7.9}$ was obtained as above. For the four positions with LL spectra in DCld 300.2–16.9, $\langle \nu I_\nu \rangle_{24}$ was derived similarly using the LL spectrum and the MIPS 24 μm filter response, times an appropriate color correction (SSC 2010b). For the LDN 1780 positions, which did not have LL spectra, we estimated the 24 μm contribution to TIR as follows. Taking the measured average value of $\langle \nu I_\nu \rangle_{7.9}/\mathrm{TIR} = 0.24 \pm 0.03$ for our sample, we used Figure 15 of Draine & Li (2007) (second panel) to infer a dust mass fraction in PAHs of
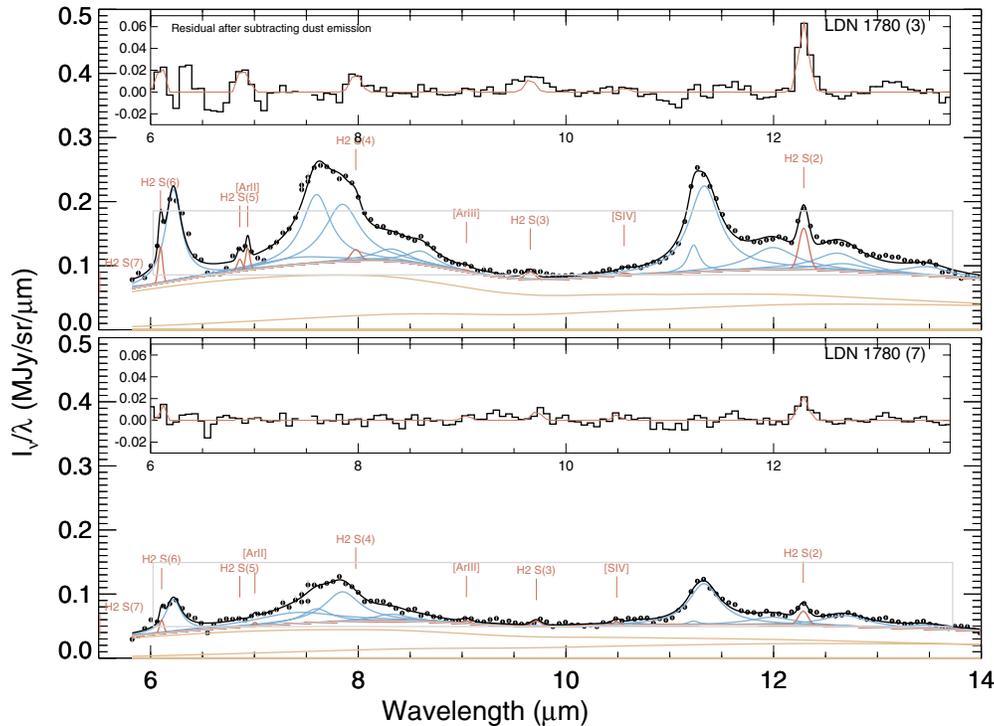
---

[11] http://ssc.spitzer.caltech.edu/dataanalysistools/cookbook/10/

Figure 3. Same as Figure 2, except that these spectra are for two positions in LDN 1780, and only cover the SL wavelength range 5.8–14.0 μm. Inset boxes cover a different range in wavelength and surface brightness per wavelength than in Figure 2 (but cover the same ranges in these two panels).

$q_{\mathrm{PAH}} = 4.6\%$. For this value of q_{PAH}, the third panel of the Figure predicts $\langle \nu I_\nu \rangle_{24}/\mathrm{TIR} \approx 0.06$. This assumes band emission relative to TIR does not vary as a function of illuminating radiation field strength U (i.e., $U \lesssim 10$, which probably holds for all cirrus clouds).

Lacking 71 and 160 μm observations toward the DCld 300.2–16.9 positions, we used ISSA 60 and 100 μm measurements, respectively, as proxies for the missing MIPS photometry. One of the HLCs in the full six-cloud sample, MBM-12 (LDN 1457) (undetected in H$_2$ S(2) emission and not observed with LL), was mapped with MIPS by Magnani et al. (2006). We computed the following rough scaling relations:

$$I_{\nu,71} = (2.30 \pm 0.08)\, I_{\nu,60} \qquad (4)$$

$$I_{\nu,160} = (4.98 \pm 0.13)\, I_{\nu,100}. \qquad (5)$$

These were derived from robust linear fits to scatter plots of $I_{\nu,71}$ versus $I_{\nu,60}$ and $I_{\nu,160}$ versus $I_{\nu,100}$ for MBM-12, using images in the given wavebands resampled to the same pixel grids. The errors in TIR are dominated by the 10% accuracy of Equation (3), as determined from model clouds heated by starlight with intensities between 0.1 and 100 times the average interstellar value (Draine & Li 2007).

3. RESULTS

3.1. Measured Surface Brightnesses

The complete 5.8–35.8 μm SL + LL spectra for the DCld 300.2–16.9 positions are displayed in Figure 2. The 5.8–14.0 μm SL spectra for the LDN 1780 positions are shown in Figure 3. We overlay on the spectra the fits to the grain and gas phase emission, and label the wavelengths of all lines in the model (regardless of detection). We detected emission in the

($v = 0$–0) 28.2 μm S(0) and 17.0 μm S(1) transitions of H$_2$ toward all four DCld 300.2–16.9 positions observed with the *Spitzer* IRS Long Low (LL) spectrograph. We detected emission in the 12.3 μm S(2) line at the $>3\sigma$ level in only six of the 34 HLC positions observed with the Short Low (SL) spectrograph: the four in DCld 300.2–16.9 observed with LL and two in LDN 1780. The 3σ detection threshold for S(2) was between 0.7 and 5.4×10^{-10} W m^{-2} sr^{-1} for the 34 observations. For the cloud positions with detectable S(2) emission, the S(0), S(1), and S(2) surface brightnesses and their uncertainties (computed by PAHFIT) are listed in Table 1, Columns 4–6.

The S(3), S(4), S(5), and S(6) lines of H$_2$ were all too faint to be detected: the integrated line strengths derived from attempting to fit the lines at the expected wavelengths were smaller than the corresponding errors in the fits. Upper limits (3σ) to the surface brightness in these transitions (Equation (2)) average about 4.2, 5.0, 5.1, and 6.8×10^{-10} W m^{-2} sr^{-1}, respectively. We print the actual limits in Columns 7–10 of Table 1. For the positions without detectable H$_2$ emission, upper limits to the S(2) through S(6) intensities are listed in Columns 4–8 of Table 2.

We list in Table 1 the dust emission surface brightness: $I_{7.9,\mathrm{PAH}}$ is in Column 11, and the TIR estimates are in Column 12. For the positions without detectable H$_2$ emission, Column 9 of Table 2 provides $I_{7.9,\mathrm{PAH}}$ measurements.

3.2. Molecular Hydrogen Excitation

We can use an excitation diagram to estimate the physical conditions in the regions producing H$_2$ rotational line emission in high-latitude translucent cirrus clouds. In Figure 4, we plot for all the Table 1 measurements the column density in rotational upper level J divided by the statistical weight, N_J/g_J, as a function of E_J/k, the upper level energy expressed as a temperature. The column densities are derived from the surface
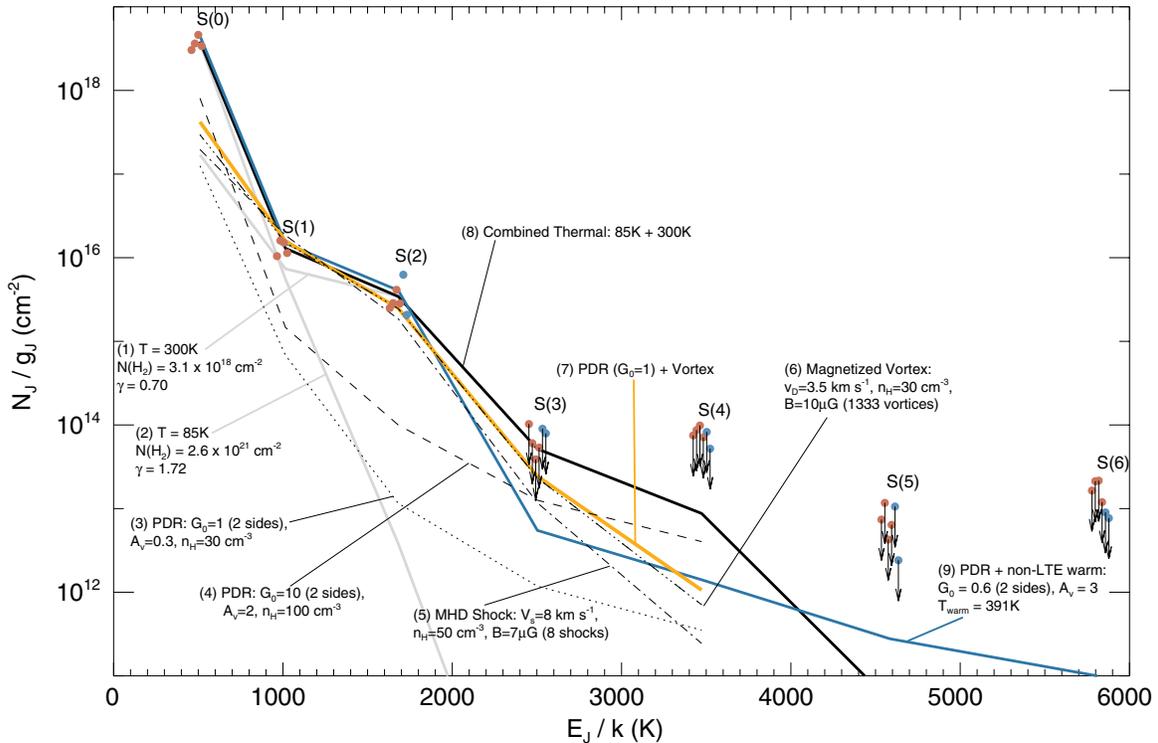
Figure 4. Excitation diagram of H$_2$ pure-rotational emission toward high-latitude cirrus clouds. Circles represent the observed measurements of DCld 300.2–16.9 (red) and LDN 1780 (blue). Transitions S(3) and higher all have 3σ upper limits, shown as downward arrows. The abscissae for each point have been shifted slightly for clarity. Superposed on the diagram are seven cloud models: (1) a thermal distribution ($T_{\mathrm{warm}} = 300$ K) with parameterized ortho/para ratio $\gamma = 0.70$ (gray); (2) a thermal distribution ($T_{\mathrm{cold}} = 85$ K) with $\gamma = 1.72$ (gray); (3) emission from a PDR illuminated on both sides by a UV flux equal to the average local interstellar value ($G_0 = 1$; Habing 1968), volume density $n_{\mathrm{H}} = 30\,\mathrm{cm}^{-3}$, and visual extinction $A_{\mathrm{v}} = 0.3$ mag (dotted); (4) PDR emission with $G_0 = 10$, $n_{\mathrm{H}} = 100\,\mathrm{cm}^{-3}$, and $A_{\mathrm{v}} = 2.0$ mag (dashed); (5) emission from eight MHD shocks traveling at $V_s = 8\,\mathrm{km\,s}^{-1}$ in gas with $n_{\mathrm{H}} = 50\,\mathrm{cm}^{-3}$ and magnetic field $B = 7\,\mu$G (dot-dashed); (6) emission from 1333 magnetized vortices with ion-neutral drift velocity $v_D = 3.5\,\mathrm{km\,s}^{-1}$, $n_{\mathrm{H}} = 30\,\mathrm{cm}^{-3}$, and $B = 10\,\mu$G (dot-dot-dashed); (7) the sum of the $G_0 = 1$ PDR and the vortex model (orange); (8) the sum of the 85 K and 300 K thermal distributions (solid black); and (9) the sum of a PDR with $G_0 = 0.6$ plus a warm component with $T = 391$ K, with non-LTE excitation. Models (3)–(6) are taken from Figure 3 of Falgarone et al. (2005). Model (9) is taken from B. T. Draine & J. G. Ingalls (2011, in preparation).

brightness assuming optically thin line radiation:

$$N_J = \frac{4\pi\, I_{J,J-2}}{A_{J,J-2}\, h\nu_{J,J-2}}. \tag{6}$$

Here, $I_{J,J-2}$ is the surface brightness and $A_{J,J-2}$ is the Einstein spontaneous emission coefficient in the transition from upper state J to lower state $J-2$. The statistical weights for rotational level J are $g_{J,\mathrm{even}} = 2J + 1$ for even J (para-H$_2$) and $g_{J,\mathrm{odd}} = 3(2J + 1)$ for odd J (ortho-H$_2$). In what follows we assume that excitation of vibrational levels is negligible.

Following Draine & Bertoldi (1996), we approximate the H$_2$ rotational populations by a thermal distribution,

$$N_J/g_J = a\, \exp(-E_J/kT_r), \tag{7}$$

where T_r is the "rotational temperature" describing the populations. Under conditions of local thermodynamic equilibrium (LTE) Equation (7) becomes a Boltzmann distribution, and $a = N(\mathrm{H}_2)/Z(T_r)$, the ratio of total H$_2$ column density to the partition function. Under non-equilibrium conditions, the ortho- and para-H$_2$ can take on separate a values, a_{ortho} and a_{para}. One way to characterize the relative populations in ortho and para states is the (Draine & Bertoldi 1996) ortho to para ratio

$$\gamma = 3a_{\mathrm{ortho}}/a_{\mathrm{para}}. \tag{8}$$

As those authors note, γ is not necessarily the column density ratio of ortho- and para-H$_2$, but rather a parameterization of

that ratio that includes the ratio of partition functions of the two types of molecular hydrogen. It has the advantage that under conditions of LTE ($a_{\mathrm{ortho}} = a_{\mathrm{para}}$), $\gamma = 3$, regardless of temperature.

The observed excitation diagram can be used to estimate physical conditions in the S(0) to S(2)-emitting gas. Using Equation (7), we note that for constant values of T_r and a, a plot of N_J/g_J versus E_J/k with logarithmically scaled ordinate will yield a straight line with slope equal to $-1/T_r$ (multiplied by $1/\log_{10}(e)$ if the ordinate is log base 10). As is typical for other measurements of H$_2$ rotational populations in diffuse gas (e.g., Rachford et al. 2001; Falgarone et al. 2005; Goldsmith et al. 2010; Jensen et al. 2010), our data do not fall on a single straight line. Here, we simply determine two excitation temperatures consistent with the three lines available. The result is somewhat arbitrary and not unique, but nevertheless is instructive.

We find that a "cold" component with excitation temperature $T_{\mathrm{cold}} = 85$ K and a "warm" component with $T_{\mathrm{warm}} = 300$ K are consistent with the data. This simple model, with $N(\mathrm{H}_2) = 2.6 \times 10^{21}\,\mathrm{cm}^{-2}$ in the cold component and $N(\mathrm{H}_2) = 3.1 \times 10^{18}\,\mathrm{cm}^{-2}$ in the warm component, reproduces the level populations in the $J = 2$, 3, and 4 levels (corresponding to the S(0), S(1), and S(2) transitions) and the upper limits in $J = 5$ and above. We overlay on Figure 4 the excitation diagram for each thermal component (gray curves), as well as the sum of the two components (solid black). The model predicts a $J = 5$ population that is right at the upper limit we have measured. This is not a concern, because the critical densities for $J = 3$, 4, and 5 are high enough that
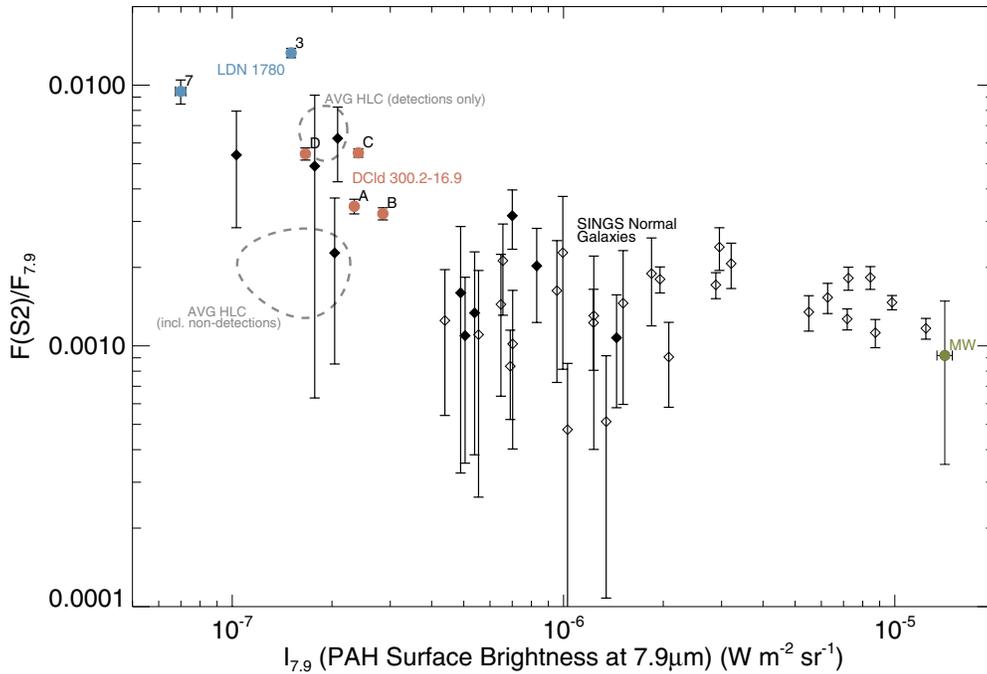
Figure 5. Ratio of the H_2 S(2) to 7.9 μm PAH flux as a function of the 7.9 μm surface brightness, for Milky Way and extragalactic sources. Red circles (A–D) are our DCld 300.2–16.9 HLC cirrus detections; blue circles (3, 7) are the LDN 1780 detections. The diamonds are Roussel et al. (2007) data for SINGS galaxies with non-active nuclei (filled diamonds are dwarf galaxies and open diamonds are galaxies with purely star-forming nuclei). The green circle (MW) is an estimate for the Falgarone et al. (2005) Milky Way galactic plane line of sight ($A_v = 30$). Dashed ellipses (pinched due to the logarithmic scaling of the axes) indicate the average $\pm 1\sigma$ for two samples of high-latitude clouds: (1) the six S(2)-detected positions and (2) the full set of 34 positions observed with SL, including nondetections.

the $J = 5$ level will be sub-thermally excited (at $T = 70$ K, $n_{crit}(H_2) = 900$, 2×10^4, and 3×10^5 cm^{-3} for $J = 3$, 4, and 5). Thus, the gas temperature would actually have to be higher than $T = 300$ K to reproduce the populations of $J = 5$ predicted by our thermal model.

In the model, we assume an ortho to para column density ratio of $N_{ortho}/N_{para} = 0.7$ for both the cold and warm components. This is based on the observed column density ratio between the $J = 1$ and 0 levels toward HD 102065 (Nehmé et al. 2008b), about 3°.4 away from the nearest position in Table 1. It seems reasonable to take the same ortho/para column density ratio for both components, on the theory that it is the cool gas that occasionally gets heated to $T = 300$ K, keeping the relative amounts of ortho and para H_2 constant. The *parameterized* ratio, γ, which measures departures from equilibrium (defined by $\gamma = 3$), is obtained by summing the predicted odd and even J Boltzmann factors over all possible rotational levels (including $J = 0$ and 1, which do not radiate), and taking the ratio. This yields $\gamma_{cold} = 1.72$ and $\gamma_{warm} = 0.70$ for our thermal model.

The two-temperature model ($T_{cold} = 85$ K and $T_{warm} = 300$ K) presented here is an oversimplification. In reality there will be a range of temperatures present, with much of the H_2 column density at $T < 85$ K (based on *FUSE* absorption measurements toward 38 translucent lines of sight, the mean $J = 1$ to $J = 0$ rotational temperature is 67 K; see Rachford et al. 2009), and some material at temperatures between 85 K and T_{warm} required to account for the observed excitation of $J = 2$.

3.3. Comparison with Measurements of the Disks of Galaxies

To answer the question of whether translucent gas is a significant source of galaxian H_2 emission, we compare the H_2 and dust emission measurements with the Roussel et al. (2007) SINGS galaxy sample and a measurement toward the mid-plane of the MW. We plot the flux ratios $F(S2)/F_{7.9,PAH}$

as a function of the surface brightness $I_{7.9,PAH}$ for the six HLC positions in Figure 5. (Since the solid angles of the H_2 and PAH measurements are the same, the surface brightness ratio equals the flux ratio.)

We also plot the SINGS extragalactic measurements of $F(S2)/F_{7.9,PAH}$ versus $I_{7.9,PAH}$ in galaxies without active nuclei (Roussel et al. 2007). We derived 7.9 μm surface brightnesses for this sample by dividing the reported Roussel et al. IRAC band 4 fluxes corrected for stellar emission by the solid angle for each galaxy observation.

We add a final data point to Figure 5: the *ISO* SWS detection of S(2) along a direction in the mid-plane of the MW ($\ell, b = 26°.46, 0°.09$; Falgarone et al. 2005). Lacking an IRAC 7.9 μm measurement or its equivalent for this position, we scaled the *IRAS* 12 μm measurements (IRIS processing; Miville-Deschênes & Lagache 2005) for the MW position to the average 7.9 μm/12 μm ratio derived from HLC synthetic photometry (7.9 μm) and IRIS measurements (12 μm). We fit a least squares bisector line (Isobe et al. 1990) to the 7.9 and 12 μm measurements and used the slope as the nominal scale factor, $I_{7.9,PAH}/I_{12,IRIS}$, to multiply by the 12 μm MW measurement. We estimated the error in the predicted $I_{7.9,PAH}(MW)$ value using the standard deviation in the six measured HLC values of the $I_{7.9,PAH}/I_{12,IRIS}$ ratio (after subtracting the bisector fit y-intercepts). Multiplying this by $I_{12,IRIS}(MW)$ gives an error in $I_{7.9,PAH}$ (MW). This error is probably an underestimate, since it ignores possible systematic differences in the PAH spectra of HLC and MW populations.

The six HLC positions have higher values of the $F(S2)/F_{7.9,PAH}$ ratio than the MW mid-plane and all but three of the SINGS non-active galaxies. The average $F(S2)/F_{7.9,PAH}$ ratio for the detected sample is $(6.7 \pm 1.6) \times 10^{-3}$. For the Roussel et al. (2007) SINGS sample the ratio averages $(2.9 \pm 0.6) \times 10^{-3}$ for dwarf galaxies, $(1.44 \pm 0.09) \times 10^{-3}$ for galaxies with
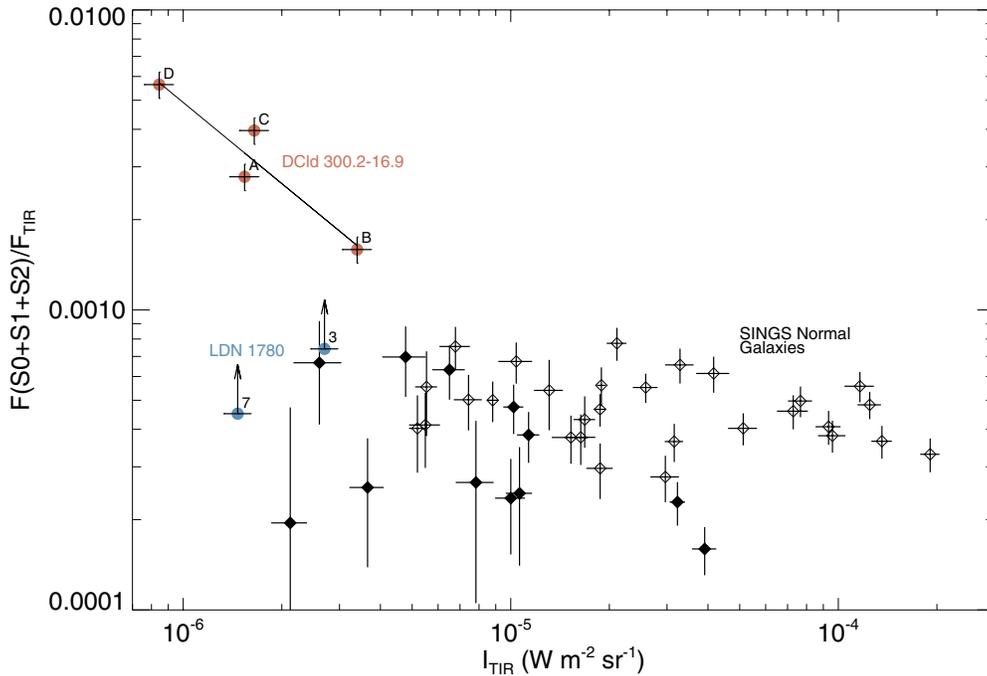
Figure 6. Ratio of the total rotational H_2 flux to TIR flux, as a function of the TIR surface brightness. Red circles (A–D) are our DCld 300.2–16.9 cirrus detections, blue circles (3 and 7) are lower limits for LDN 1780, and diamonds are Roussel et al. (2007) data for SINGS galaxies with non-active nuclei (see Figure 5). A power law fit to the DCld 300.2–16.9 points (gray line) yields $F(S0 + S1 + S2)/F_{TIR} = 2.0 \times 10^{-8}$ TIR$^{-0.9}$.

purely star-forming nuclei, and $(1.8 \pm 0.2) \times 10^{-3}$ for the combined set. For the Falgarone et al. (2005) MW position, the ratio is $(1.0 \pm 0.6) \times 10^{-3}$. For the complete 34-position HLC sample, 27 lines of sight showed PAH emission in the 7.9 μm band but no S(2) emission (Table 2). If we include all 7.9 μm detections in the HLC average, the ensemble has a ratio of $(2.0 \pm 0.8) \times 10^{-3}$, which is identical within the error bars to the full SINGS average and the MW data point. (We estimated the average S(2) intensity for the complete sample using a spectrum produced by co-adding the background-subtracted IRS spectral images for all 34 positions.) In the following section, we discuss the possibility that translucent cirrus comprises a significant component of galaxian H_2 rotational emission.

A useful diagnostic of the relative strength of H_2 emission to absorbed interstellar radiation is the ratio of the flux in the S(0), S(1), and S(2) lines to the total infrared flux, $F(S0 + S1 + S2)/F_{TIR}$. We plot in Figure 6 this ratio as a function of I_{TIR} for the four DCld 300.2–16.9 positions with LL spectra, as well as the two lower limits from the LDN 1780 S(2) data. Here the DCld 300.2–16.9 points lie well above the extragalactic measurements. The average value of $F(S0 + S1 + S2)/F_{TIR}$ for DCld 300.2–16.9 is $(3.5 \pm 0.9) \times 10^{-3}$. For the SINGS data, the ratio is $(3.7 \pm 0.6) \times 10^{-4}$ for dwarf nuclei, $(4.8 \pm 0.2) \times 10^{-4}$ for pure star-forming nuclei, and $(4.5 \pm 0.8) \times 10^{-4}$ for the complete sample. It is notable that for the LDN 1780 positions, $F(S2)/F_{TIR}$ alone is of the same order of magnitude as $F(S0 + S1 + S2)/F_{TIR}$ for the SINGS galaxies. Unlike extragalactic H_2 emission, the H_2 emission for HLCs seems only loosely correlated (if at all) with the infrared flux: a power law fit to the DCld 300.2–16.9 data in Figure 6 has $I(S0 + S1 + S2) \propto I_{TIR}^{0.1}$.

4. DISCUSSION

We have detected molecular hydrogen rotational emission toward six of 34 translucent high Galactic latitude cirrus positions. The $(v = 0\text{–}0)$ S(0), S(1), and S(2) transitions of H_2 originate from energy levels that are 510 K, 1015 K, and 1682 K above the ground state. How are these levels excited in the translucent ISM, which is embedded in cold H I gas with a median temperature of $\sim$70 K (Heiles & Troland 2003)? Why do some locations show S(2) emission and others do not? Do we expect a significant amount of H_2 cirrus emission throughout the Galaxy, and by extension in other normal galaxies? These are the main questions we will try to address here.

4.1. The Environment of the Clouds

We first examine the environment of the two clouds we have detected, DCld 300.2–16.9 and LDN 1780, focusing on aspects of the clouds that may explain the H_2 emission we have observed. Both clouds are thought to be part of the cold neutral medium (CNM) that defines the boundary of the 30–100 pc diameter local cavity (LC) of low-density ($n \lesssim 0.1\,\mathrm{cm}^{-3}$) gas in which the Sun resides (Welsh et al. 2010). The clouds also both happen to be on the interface between the LC and the superbubble surrounding the Scorpius-Centaurus (Sco-Cen) OB association (de Geus 1992), albeit on opposite sides. Southeast of the superbubble center (in Galactic coordinates), DCld 300.2–16.9 is located along the line of sight to the Chamaeleon molecular cloud, but is probably closer than the $\sim$150 pc distance of the main complex (Mizuno et al. 2001; Nehmé et al. 2008a). Mizuno et al. (2001) deduced that the cloud is at a distance of 70 ± 15 pc from the Sun, based on the location of T Tauri star T Cha, toward which the cloud peak of CO emission has the same radial velocity. The cloud is thus $\sim$30 pc from the center of the Lower Centaurus Crux (LCC) subgroup of Sco-Cen. Northwest of the superbubble center, LDN 1780 ($\ell, b = 358°9, 36°9$) is about 100 pc from the Sun (Franco 1989; Lallement et al. 2003) and is thus $\approx$70 pc away from the center of the Upper Scorpius (US) subgroup of Sco-Cen (Laureijs et al. 1995; de Geus 1992). Arrows pointing from the clouds to the centers of the LCC and US subgroups are drawn in

Figure 1. Projected on the plane of the sky, LDN 1780 is $\approx 75°$ away from DCld 300.2–16.9, so the clouds are separated by at least 100 pc.

In terms of their processing of the ISRF, both clouds have 60/100 μm colors and C II cooling intensities that are typical of translucent Galactic cirrus, and have been modeled as objects with visual extinctions $A_v \sim 1$ magnitude and ISRF intensities $G_0 \sim 1$, in units of the Habing (1968) flux (Ingalls et al. 2002; Juvela et al. 2003; Nehmé et al. 2008b).

We estimate that the Table 1 positions have extinctions of from 1 to 3 mag. For DCld 300.2–16.9, the Mizuno et al. (2001) ^{12}CO map has integrated intensities $I_{CO} \sim 10$ K km s^{-1} near our positions, which yields a molecular column density of $N(H_2) \sim 2 \times 10^{21}$ cm^{-2}, if we use a typical conversion factor between I_{CO} and $N(H_2)$ (e.g., see Liszt et al. 2010). Using the well-established relationships $N_H/E_{B-V} = 5.8 \times 10^{21}$ cm^{-2} and $A_v/E_{B-V} = 3.1$ in diffuse gas (Bohlin et al. 1978; Rachford et al. 2009), this gives $A_v \approx 1.1$ mag (this is probably an underestimate since it does not count H I). The LDN 1780 positions have measured visual extinctions of $A_v \approx$ 2–3 mag (del Burgo & Cambrésy 2006), which corresponds to a total gas column density of $N_H \sim (3.7–5.6) \times 10^{21}$ cm^{-2}. Alternatively, the average 100 μm surface brightness toward all detected DCld 300.2–16.9 and LDN 1780 positions is 13.4 MJy sr^{-1}. Using the Boulanger et al. (1996) conversion $N(H I) \approx 2 \times 10^{20}$ cm^{-2} $(I_{100}/$ MJy sr$^{-1})$ yields a column density of 2.7×10^{21} cm^{-2}, or $A_v = 1.4$ mag.

The portion of DCld 300.2–16.9 in front of HD 102065, about $3°.4$ (4.2 pc) away from the nearest position in Table 1, has been studied in absorption of H_2, CH^+, and many other species by Gry et al. (2002) and Nehmé et al. (2008a). A model of the direction toward this star can reproduce most of the observations if $A_v \sim 0.7$ and $G_0 \sim 0.7$ (Nehmé et al. 2008b). However, the populations in the H_2 $J > 2$ rotational levels require excitation beyond that produced by any reasonable incident radiation field to explain the observed absorption. The authors concluded that a warm ($T \sim 250$ K), out-of-equilibrium gas is also present along the line of sight. Nehmé et al. (2008a) posited that the cloud's current state is the result of an interaction between a supernova blast wave from one or more stars in the LCC subgroup and the ambient ISM, about 2–3 $\times 10^5$ yr ago.

LDN 1780 is also thought to have been affected profoundly by its proximity to the Sco-Cen association. The cloud is located between two near-parallel arcs of H I emission. The outer arc is assumed to be H I swept up by supernova explosions in the Upper Centaurus Lupus (UCL) subgroup of Sco-Cen, whereas the inner arc is believed to have been produced by the supernovae in the US subgroup (de Geus 1992). Tóth et al. (1995) proposed a scenario in which a shock front propagating outward at a speed of $\sim$10–15 km s^{-1} from UCL has passed through LDN 1780. Since the loop is currently about 7 pc away from the cloud, we estimate that the cloud's interaction with the shock probably occurred $\sim 6 \times 10^5$ yr ago. Tóth et al. noted that the H I emission from LDN 1780 peaks on the lower latitude diffuse side of the cloud facing the US subgroup and the stars of the Galactic mid-plane; the CO emission peaks on the dense side of the cloud further from these sources of radiation. They argued that the cometary shape of the cloud is due to the passage of the UCL shock wave, whereas the segregation between molecular and atomic material is due to an asymmetric UV radiation field originating from the US subgroup and the Galactic mid-plane. Laureijs et al. (1995) estimated that G_0 might be as high as 3 on the diffuse side of the cloud, but may be only half as strong

on the dense side. The H_2 S(2) emission we detect is stronger toward position 3 (Table 1), which is close to the H I peak. We argue in Section 4.2 that the UV field is insufficient to produce the emission, and suggest instead that the S(2) emission results from the cloud's interaction with the supernova blast wave.

LDN 1780 is unusual among molecular clouds in that it has a significant Hα surface brightness, correlated with tracers of column density (del Burgo & Cambrésy 2006; Witt et al. 2010). Mattila et al. (2007) suggested that this could be explained by scattering of background Hα photons by dust grains, and the recent study by Witt et al. (2010) strongly supports this interpretation. The ζ Oph and δ Sco H II regions appear to be within a few tens of pc of the southern surface of LDN 1780, and represent likely sources of background Hα.

4.2. Sources of Molecular Hydrogen Excitation

In interstellar cirrus, H_2 may be excited into rotational emission via UV pumping by starlight; or via collisional excitation resulting from mechanical energy dissipation in magnetohydrodynamic (MHD) shocks (Draine et al. 1983; Flower et al. 1986), coherent vortices or intense velocity shears (Joulain et al. 1998; Falgarone et al. 2005; Godard et al. 2009), or by interaction with cosmic rays (Ferland et al. 2008). All of these sources may be present at some level in DCld 300.2–16.9 and LDN 1780.

4.2.1. UV Pumping

The ISRF is the most obvious source of H_2 excitation in cirrus clouds. FUV radiation heats the gas and dust and drives the chemistry in all translucent regions. Roussel et al. (2007) found a correlation between H_2 emission and infrared emission in the disks of SINGS normal galaxies. Since IR radiation traces the processing of starlight by dust, SINGS H_2 emission appears to be tied to the FUV radiation field. But for cirrus clouds, it is difficult to reproduce the observed H_2 emission with only the ISRF. We overlay on Figure 4 the predicted excitation in two PDR models (Falgarone et al. 2005). The first model is immersed in the Habing (1968) ISRF ($G_0 = 1$) and has gas volume density $n = 30$ cm^{-3}, and visual extinction $A_v = 0.3$ mag. The second PDR model has a larger UV flux and is denser and thicker: $G_0 = 10$, $n = 100$ cm^{-3}, and $A_v = 10$ mag. The translucent HLCs in our study are probably somewhere in between these models. Both models fall short of reproducing our observed measurements by at least a factor of 10. In another H_2 fluorescence model, that of Black & van Dishoeck (1987), the S(2) emission we observe can only be reproduced if the radiation field was increased to $G_0 \sim 30$. This would, however, result in S(3) emission at a level we would have detected. Furthermore, there is no evidence that these HLCs are heated by radiation fields greater than $G_0 \approx 3$ (Laureijs et al. 1995; Ingalls et al. 2002; Juvela et al. 2003; Nehmé et al. 2008b). So another mechanism must dominate the H_2 pure-rotational excitation.

We note that by far the brightest S(2) emission we have detected is toward position 3 of LDN 1780. This position has three times as much S(2) radiation as position 7, and also has twice as much 7.9 μm PAH emission as position 7, consistent with the PAHs on the southern side of the cloud (in Galactic coordinates) being exposed to higher starlight intensities, as predicted by Laureijs et al. (1995). The ISRF would have to be increased by a factor of more than 100, however, to account for the H_2 S(2) emission toward this position, which would boost the PAH emission by a similar factor (provided the density remained the same) and would result in detectable S(3) emission and much

brighter S(0) and S(1) lines than we observe. The highest *IRAS* $60/100 \mu$m surface brightness ratio measured toward LDN 1780 is 0.275 (Ingalls et al. 2002), which implies $G_0 \sim 2$–4. Witt et al. (2010) found that for the entire cloud, grain temperatures are in the range 14.5–16.8 K, consistent with $G_0 \sim 1$. Therefore, it is likely that most of the S(2) radiation represents the dissipation of mechanical energy that was concentrated on the south side of the cloud (like the passage of a supernova blast wave).

4.2.2. Collisional Excitation

H_2 rotational transitions can be collisionally excited into emission via shock heating (Draine et al. 1983) or turbulent dissipation (Godard et al. 2009; Falgarone et al. 2005).

What kind of shocks would be capable of powering the observed emission? The observed H_2 S(0) to S(2) line intensities sum to $I(0\text{–}2) \equiv I[S(0)] + I[S(1)] + I[S(2)] \approx 5 \times 10^{-9}$ W m^{-2} sr^{-1} (on average) at the 4 DCld 300.2–16.9 positions where emission is detected. If a fraction $f(0\text{–}2)$ of the shock power is radiated in these lines then, assuming the shock front fills the beam,

$$I(0\text{–}2) \approx \frac{1}{8\pi} \frac{1}{\cos\theta} f(0\text{–}2) \rho_0 v_s^3 \qquad (9)$$

for a strong shock, where θ is the angle between the shock normal and the line of sight, ρ_0 is the density of the pre-shock gas, and v_s is the shock propagation velocity. Thus,

$$v_s \approx 8 \text{ km s}^{-1} \left[\frac{I(0\text{–}2)}{5 \times 10^{-9} \text{ W m}^{-2} \text{ sr}^{-1}} \frac{\cos\theta}{f(0\text{–}2)} \frac{100 \text{ cm}^{-3}}{n_{\text{H},0}} \right]^{1/3}. \qquad (10)$$

Therefore, if the S(0–2) lines are major coolants, and if the line ratios are also consistent, a shock speed of order 8 km s^{-1} would be sufficient to produce the observed line fluxes. Figure 4 of Draine et al. (1983) indicates that the H_2 lines are in fact expected to dominate the cooling of $v_s = 5$–20 km s^{-1} C-type shocks propagating into gas with $n_{\text{H},0} = 100$ cm^{-3} and $B_0 = 10 \mu$G.

Matching the line ratios is a separate challenge. The $J = 3$ and $J = 4$ levels could be excited in shocks. Draine & Katz (1986) show results for shocks propagating into gas with $n_{\text{H}} = 50$ cm^{-3} and $B_0 = 7 \mu$G. For $v_s \approx 12$ km s^{-1} and $\cos\theta = 0.5$, these models reproduce the observed S(2) emission and overestimate by a factor of about 2.6 the S(1) emission. The models assumed an ortho/para ratio of 3; using a smaller ratio (e.g., $\gamma = 0.7$) could decrease the S(1)/S(2) ratio to agree with the observed values.

If such shocks are present in these clouds, one would expect to see 21 cm emission with components corresponding to both the pre-shock and post-shock material. CO ($J = 1$–0) line emission should also show pre-shock and post-shock components. Such signatures have yet to be detected.

Published shock models fail to predict the S(0) emission we observe toward HLCs without overestimating the S(1) and/or S(2) lines. The very large column density $N(J = 2) = 1.5 \times 10^{19}$ cm^{-2} appears to require a large filling factor of H_2 gas with relatively cool temperatures. For thermal excitation we reproduce the S(0) emission if most of the gas has an excitation temperature of $T = 85$ K (Figure 4, black curve).

One approach to increasing the $J = 2$ population relative to $J = 3$ and 4, while still reproducing the overall column densities, has been to posit multiple superimposed, randomly

oriented shock waves. Both Gredel et al. (2002) and Falgarone et al. (2005) applied the MHD shock model of Flower & Pineau des Forêts (1998) to measurements of molecular lines in diffuse clouds and found that many of the observations could be explained by ensembles of shock waves. For comparison with our data, we display in Figure 4 (dash-dotted curve) the sum of eight shocks traveling with velocity $v_s = 8$ km s^{-1} into a medium of $n_{\text{H}} = 50$ cm^{-3} and $B = 7 \mu$G (models taken from Figure 3 of Falgarone et al. 2005). Falgarone et al. found that, per magnitude of visual extinction, 3.2 shocks with $v_s = 8$ km s^{-1} can reproduce their S(1) and higher emission from the diffuse medium. This is nearly the same "shock fraction" we need for the S(1) and S(2) data toward DCld 300.2–16.9 and LDN 1780 (our sample has $A_v \approx 2$ mag, giving four shocks per magnitude). Since the shocks each have a column density $N_{\text{sh}} = 1.5 \times 10^{17}$ cm^{-2} of hot gas, the mass fraction of shocked gas in this model is about 0.06%. The model $J = 3$ and $J = 4$ column densities are reasonably well matched to the data, but $J = 2$ is still insufficiently populated. Indeed, referring to the Draine & Katz (1986) models, even a $v_s = 5$ km s^{-1} shock overproduces S(1) emission relative to S(0) by a factor of eight, so the $J = 2$ levels remain a problem to reproduce for shock models.

Although shocks provide one mechanism for localized heating, it has also been proposed that intermittent dissipation of turbulence can produce localized, transient pockets of hot gas (Joulain et al. 1998; Falgarone et al. 2005; Godard et al. 2009). We show in Figure 4 the excitation diagram for 1300 vortices, scaled from Figure 3 of Falgarone et al. (2005) (dot-dot-dash curve). The vortices have ion-neutral drift velocity $v_D = 3.5$ km s^{-1}, $n_{\text{H}} = 30$ cm^{-3}, and $B = 10 \mu$G. The model has very similar H_2 excitation to the multiple shock model described above, although it has a lower ortho/para ratio which gives a slightly better match to our S(1) and S(2) data. We get the same "vortex fraction" as Falgarone et al., $\sim$700 vortices per magnitude of visual extinction. The vortex column density of $N_{\text{vor}} = 1.7 \times 10^{14}$ cm^{-2} gives a mass fraction in the vortices of about 0.01%.

Since all cirrus is exposed to the ISRF, a more realistic model contains both UV and collisional heating. We display in Figure 4 the sum of the $G_0 = 1$ PDR and the $v_D = 3.5$ km s^{-1} vortex models (orange curve). The S(0) line remains underpredicted, by about a factor of 10.

We have computed an additional model that reproduces the H_2 level populations quite well, even though it lacks a specific mechanism for heating the warm molecular gas (B. T. Draine & J. G. Ingalls 2011, in preparation). This model is plotted in blue in Figure 4. It consists of a plane-parallel molecular cloud with an H I layer (PDR) on both front and back sides, superimposed with a zone of warm gas. The PDR portion of the slab obtains a uniform gas pressure $P/k = 4000$ cm^{-3} K (consistent with pressure measurements in the ISM based on [C I] excitation—see Jenkins & Tripp 2011), and is embedded in a radiation field equal to 0.6 times the Habing (1968) energy density at 1000 Å. The warm zone is assumed to have been suddenly heated, so that the ortho/para ratio has not had time to reach equilibrium corresponding to T_{warm}. Collisional excitation of the H_2 rotational levels is calculated using state-to-state rates. The data are best fit by $T_{\text{warm}} = 391$ K, an ortho/para column density ratio in both the warm and cool gas of 0.15, and a warm H_2 column density $N_{\text{warm}}(H_2) \approx 5.15 \times 10^{19}$ cm^{-2}, which is about 2% of the total H_2 column density in the model. The bulk of the H_2 emission in this model is not due to radiative pumping;

more than 97% of the $J = 2, 3$, and 4 excitation is produced in the warm component.

4.3. H_2 Excitation in the Supernova-Driven ISM

In summary, the (somewhat speculative and incomplete) scenario we envision is one in which CNM molecular clouds immersed in the ISRF of intensity $G_0 \sim 1$ are subjected to a large-scale injection of mechanical energy and dissipate that energy intermittently on smaller scales via shocks, or perhaps in localized transient turbulent dissipation regions (TDRs; Godard et al. 2009) such as vortices or velocity shears (or some combination thereof). The H_2 S(0) – S(2) lines are presumed to be mainly excited by collisions in hot regions, heated by mechanical energy dissipation. The gas is initially cold ($T \lesssim 100$ K), and in the shielded interior of a cloud the ortho/para ratio may be very low. When dissipational heating occurs, local temperatures temporarily reach values near 1000 K, and ortho/para rises. If the source of large-scale mechanical energy is not refreshed somehow, the fraction of warm gas will decrease until the line radiation is no longer detectable.

Since both clouds in this study are thought to have been affected by supernova explosions from the Sco-Cen OB association about $(2–6) \times 10^5$ yr ago (Tóth et al. 1995; Nehmé et al. 2008a), we surmise that portions of the medium are still dissipating the energy deposited from those 100 pc scale blast waves. For this scenario to hold, the time to dissipate the gas turbulent kinetic energy must be larger than the time since blast wave impact. Using the total H_2 S(0–2) intensity from the DCld 300.2–16.9 positions, $I(0–2) \approx 5 \times 10^{-9}$ W m^{-2} sr^{-1}, we can calculate the H_2 cooling rate per H atom:

$$\Lambda_H = \frac{4\pi \, I(0–2)}{N_H} = 3.1 \times 10^{-33} \text{ W (H atom)}^{-1}$$
$$\times \left(\frac{I(0–2)}{5 \times 10^{-9} \text{ W m}^{-2} \text{ sr}^{-1}}\right) \left(\frac{2 \times 10^{21} \text{ cm}^{-2}}{N_H}\right). \quad (11)$$

The turbulent kinetic energy per proton is

$$E_{kin,H} = 1.4 \times \frac{3}{2} m_p \sigma_v^2$$
$$= 3.2 \times 10^{-20} \text{ J (H atom)}^{-1} \left(\frac{\sigma_v}{3 \text{ km s}^{-1}}\right)^2, \quad (12)$$

where m_p is the proton mass, σ_v is the Gaussian standard deviation of the observed velocity distribution, and the factor 1.4 accounts for helium. Using Parkes Galactic All Sky Survey (Kalberla et al. 2010) H I observations toward DCLd 300.2–16.9, we measure $\sigma_v \approx 3$ km s^{-1}. Dividing the turbulent energy by the cooling rate gives the dissipation time:

$$t_{dis} = \frac{E_{kin,H}}{\Lambda_H} = 3 \times 10^5 \text{ yr} \left(\frac{\sigma_v}{3 \text{ km s}^{-1}}\right)^2$$
$$\times \left(\frac{5 \times 10^{-9} \text{ W m}^{-2} \text{ sr}^{-1}}{I(0–2)}\right) \left(\frac{N_H}{2 \times 10^{21} \text{ cm}^{-2}}\right). \quad (13)$$

Thus, the time over which the observed H_2 emission can dissipate the available turbulent kinetic energy is of the same order of magnitude as the time since supernova impact.

This dissipation time might be an upper limit, since the H_2 lines are not the only coolant of the warm gas. Above about 200 K the 63 μm fine-structure line of neutral oxygen [O I] can account for a significant fraction of the cooling; and below

200 K the 158 μm line of ionized carbon [C II] can dominate the cooling (Falgarone et al. 2007). Our non-LTE+PDR model predicts 63 μm [O I] and 158 μm [C II] emission from the $T = 391$ K warm zone of $\approx 1 \times 10^{-9}$ W m^{-2} sr^{-1} each, which increases the total cooling by about 40% over that due to H_2 emission alone, leading to a corresponding decrease in the estimated dissipation time. (The model assumes an oxygen abundance of 4×10^{-4} and a carbon abundance of 1×10^{-4}.) For DCld 300.2–16.9, the reduced dissipation time is about the same as the time since supernova impact deduced by Nehmé et al. (2008a; $(2–3) \times 10^5$ yr, based on the time it took the observed 10 km s^{-1} H I streaming motions to create the cloud's 2.4 pc tail). The detection of [O I] 63 μm emission at the $\sim 10^{-9}$ W m^{-2} sr^{-1} level would help to confirm our assertion that the H_2 emission we observe originates in anomalously warm regions, since the model predicts about six times as much [O I] flux in the warm zone as in the PDR. Nearly all of the HLC positions in our study show [C II] 158 μm emission (Ingalls et al. 2002) at a level consistent with the PDR part of the model. Since only 5% of [C II] emission is expected to originate in the 391 K zone, this cannot likewise be used to corroborate the existence of warm material.

For LDN 1780, we have inferred a time of 6×10^5 yr since supernova impact, which is somewhat larger than the estimated dissipation time. We lack S(0) or S(1) measurements toward this cloud, however, so it is not clear that t_{dis} estimated from the DCld 300.2–16.9 total S(0–2) intensity is appropriate for LDN 1780.

The timescale to expend the available kinetic energy can also *increase* by a factor of a few or more, depending on the specific mechanism of dissipation. If the H_2 emission is primarily the result of large-scale shocks, then dissipation will begin soon after energy injection. If the emission is caused by turbulent dissipation at small scales, however, then any large-scale mechanical energy input will take additional time to flow from the input scale to the dissipation scale. For a Kolmogorov-like turbulent spectrum the dissipationless cascade will be dominated by the large-scale turnover time, L/σ_v. Given a velocity dispersion of 3 km s^{-1} and an input size scale of $L \sim 1$ pc, this turnover time is $\approx 3 \times 10^5$ yr, of order the dissipation time itself.

In general, a given spot in the Galactic disk experiences a supernova explosion within 100 pc once every $\sim 10^6$ yr. Since any energy deposited would dissipate in $t_{dis} \approx 3 \times 10^5$ yr, our scenario provides a natural explanation for the statistical dearth of rotationally excited H_2 in other translucent regions in our 100 pc neighborhood (we only detected 12.3 μm emission toward two out of six HLCs observed). The case of LDN 183, considered part of the same molecular complex as LDN 1780 (Laureijs et al. 1995; Lallement et al. 2003), lends plausibility to this picture. LDN 183, which lacks detectable S(2) emission, is *outside* the arc of the H I loop that passed through LDN 1780 (Tóth et al. 1995) $\sim 6 \times 10^5$ yr ago, and so perhaps has not yet been subjected to the same large-scale energy injection that excited the S(2) emission we see toward LDN 1780.

4.4. A New Source of H_2 Photons from Galaxies?

DCld 300.2–16.9 and LDN 1780 could be templates for an as-yet undefined "translucent" source of H_2 pure-rotational emission from the disks of all non-active galaxies. For a large sample of galaxies, Roussel et al. (2007) found that the ratio between the total H_2 flux in the S(0)–S(2) transitions and the PAH emission at 7.9 μm, F(S0–S2)/$F_{7.9,PAH}$, was remarkably constant. The ratio was constant regardless of whether the

IR emission was dominated by cirrus or high-intensity PDRs (their Figure 9), which they took to signify that the emission from both PAHs and H_2 is caused chiefly by FUV excitation in PDRs. But when we compare our *Spitzer* $F(S2)/F_{7.9,PAH}$ measurements to the Roussel et al. data (Figure 5), we see that cirrus positions are paradoxically *brighter* in S(2) emission (relative to PAH emission), by a factor of four (on average). Thus, translucent material appears to be at least as effective at producing rotationally excited H_2 molecules (per PAH-exciting photon) as PDRs surrounding H II regions.

Including the S(0) and S(1) emission for DCld 300.2–16.9 and estimating the TIR emission yields S(0–2)/TIR values that are ~10 times higher on average than the non-active galaxy ensemble. This implies that the overall H_2 excitation in translucent cirrus is higher per unit of *total* energy absorbed by dust from the ambient radiation field. Qualitatively, this is not a controversial statement; Black & van Dishoeck (1987) showed that regions with $G_0/n \ll 1$ are more efficient at radiatively exciting H_2 than regions with $G_0/n \gtrsim 1$, because when G_0/n is high the resulting low H_2 abundance means that the 1110–912 Å UV photons that might pump H_2 are instead absorbed by dust grains. But as we have shown, the S(0) to S(2) emission we observe is far greater than that expected from PDR models, requiring us to invoke collisional excitation in anomalously warm regions.

The HLCs in which we have detected S(2) emission have a greater concentration of rotationally warm gas than the integrated disks of galaxies—including the MW. The integrated S(2) emission from a column of material equivalent to ~30 mag of visual extinction in the MW (Falgarone et al. 2005) is indistinguishable in Figure 5 from the SINGS star-forming galaxies. One-half of the mass in the MW column is calculated to be in diffuse gas (Falgarone et al. 2005), so it is reasonable to expect that other galaxies likewise have a significant mass of diffuse gas that emits S(2) radiation. Indeed, there is evidence that cold gas with detectable S(2) emission, if not common, may nevertheless be present throughout the disks of normal galaxies. As mentioned, the data are consistent with other measurements of nearby molecular lines of sight: analysis of both the emission from Taurus (Goldsmith et al. 2010) and local absorption toward stars measured with *FUSE* (Rachford et al. 2001; Gry et al. 2002) shows similar excitation conditions to those reported here (Section 3.2). In addition, recent measurements of H_2 in nearby galaxies (Laine et al. 2010; Stacey et al. 2010) yield S(0)/S(1) rotational temperatures that are similar to those we measure (~100–150 K). These temperatures do not vary across the disks of the galaxies, despite the fact that star formation indicators decrease radially, suggesting a component of excitation that is unrelated to PDRs surrounding O and B stars.

Assume that the 34-position high-latitude cloud sample is representative of all translucent gas in the Galaxy. If so, then the average $F(S2)/F_{7.9,PAH}$ ratio for all positions, including nondetections, estimates the overall Galactic ratio for such material. A gray dashed ellipse in Figure 5 represents this average, and is centered on practically the same value of $F(S2)/F_{7.9,PAH}$ as the SINGS average. It is therefore plausible that translucent clouds integrated over the disks of galaxies represent a significant source of the H_2 pure-rotational emission.

4.5. Future Work to Characterize Warm H_2 in Cirrus Clouds

We have proposed a rather speculative scenario to explain the S(0) through S(2) emission we detect toward two translucent cirrus clouds. We used models of radiative and mechanical heating to estimate the conditions that could reproduce the observations. Knowledge of the superbubble environment of the clouds lends credence to the idea that extra mechanical energy is available to raise enough H_2 to the $J = 4$ state. The processes responsible for the heating remain uncertain. TDRs (Godard et al. 2009) may be able to produce strong localized heating, but more complete theoretical models of how this may proceed in magnetized interstellar gas remain to be developed. If shock waves are responsible for the heating, it should be possible to identify other evidence for the presence of a shock, such as separate radial velocities in the pre-shock and post-shock regions.

New observations are also required to confirm our interpretation of the data, especially our assertion that H_2 rotational emission from cirrus is widespread in normal galaxies, and that cirrus gas is a major source of the integrated emission. H_2 absorption line studies with *FUSE* have already established the ubiquity of H_2 in $J = 2, 3, 4$, and 5 at levels in excess of what can be explained by UV pumping (Wakker 2006; Gillmon et al. 2006)—see Figure 31.4 in Draine (2011). The Cosmic Origins Spectrograph on the *Hubble Space Telescope* can make additional H_2 absorption line measurements in diffuse and translucent clouds when suitable background UV sources are available. Later in this decade, it will be possible to measure the IR line emission from rotationally excited H_2 using both the *James Webb Space Telescope* and the proposed *Space Infrared Telescope for Cosmology and Astrophysics*. Other tracers of warm diffuse molecular gas, such as CH^+ and SH^+ (e.g., Menten et al. 2011; Falgarone et al. 2010a, 2010b), and [O I], can also be used to study the heating processes in diffuse and translucent material.

5. CONCLUSIONS

We have detected molecular hydrogen pure-rotational ($v = 0$–0) emission up to the S(2) transition toward six positions in two nearby high Galactic latitude translucent cirrus clouds (HLCs). Excitation analysis for the three available lines show that a small amount ($\lesssim 2\%$) of the gas is rotationally warm ($T_r \gtrsim 300$ K). PDR models with $G_0 = 0.6$–10 are unable to account for the observed emission, whereas models of shocks or TDRs can reproduce the S(1) and S(2) measurements. Both clouds have likely been impacted by shock waves from the Scorpius-Centaurus OB association about 2–6×10^5 yr ago, which may have injected sufficient mechanical energy to excite the H_2 rotational levels. Four other nearby HLCs, which are not so situated, did not show detectable S(2) lines. This picture is still speculative, however, and requires robust modeling to confirm it.

Prior to the *Spitzer Space Telescope*, published observations of molecular hydrogen in the diffuse ISM were confined to UV absorption measurements (for example, see Rachford et al. 2001, 2002; Gry et al. 2002; Gillmon et al. 2006; Wakker 2006; Rachford et al. 2009; Jensen et al. 2010) or a measurement of the emission along an extensive ($A_v \sim 30$ mag) line of sight in the Galactic mid-plane (Falgarone et al. 2005). During its cryogenic lifetime, *Spitzer* has enabled a new way of looking at the neutral ISM, confirming the notion that a significant amount of warm molecular gas exists within the cold medium, both within our own Galaxy (this paper; Goldsmith et al. 2010), and in external galaxies (Laine et al. 2010; Stacey et al. 2010). We propose that rotationally warm gas inside cold clouds is a feature of the disks of all normal galaxies. While it may not be common (less than 20% of our sample had detectable H_2 emission, and at most 2%

of the column density toward the detected positions is warm gas), it appears to be widespread. The enhanced H_2 flux relative to dust emission in HLCs compared with the inner disks of the SINGS galaxies, together with the known ubiquity of $A_v \sim 1$ material in the Galactic plane (Polk et al. 1988), requires that the translucent cirrus be taken into account when interpreting the H_2 rotational lines in the disks of all non-active galaxies.

Facility: Spitzer

REFERENCES

Bertoldi, F., Draine, B. T., Rosenthal, D., et al. 2000, in IAU Symp. 197, Astrochemistry: From Molecular Clouds to Planetary Systems, ed. Y. C. Minh & E. F. van Dishoeck (Cambridge: Cambridge Univ. Press), 191
Black, J. H., & van Dishoeck, E. F. 1987, ApJ, 332, 412
Bohlin, R. C., Savage, B. D., & Drake, J. F. 1978, ApJ, 224, 132
Boulanger, F., Abergel, A., Bernard, J.-P., et al. 1996, A&A, 312, 256
de Geus, E. J. 1992, A&A, 262, 258
del Burgo, C., & Cambrésy, L. 2006, MNRAS, 368, 1463
Draine, B. T. 2011, Physics of the Interstellar and Intergalactic Medium (Princeton, NJ: Princeton Univ. Press)
Draine, B. T., & Bertoldi, F. 1996, ApJ, 468, 269
Draine, B. T., Dale, D. A., Bendo, G., et al. 2007, ApJ, 663, 866
Draine, B. T., & Katz, N. 1986, ApJ, 310, 392
Draine, B. T., & Li, A. 2007, ApJ, 657, 810
Draine, B. T., Roberge, W. G., & Dalgarno, A. 1983, ApJ, 264, 485
Falgarone, E., Godard, B., Cernicharo, J., et al. 2010a, A&A, 521, L15
Falgarone, E., Ossenkopf, V., Gerin, M., et al. 2010b, A&A, 518, L118
Falgarone, E., Pety, J., Hily-Blant, P., & Pineau des Forêts, G. 2007, in Molecules in Space & Laboratory, ed. J. L. Lemaire & F. Combes, 92 (S. Diana, Paris)
Falgarone, E., Verstraete, L., Pineau des Forêts, G., & Hily-Blant, P. 2005, A&A, 433, 997
Ferland, G. J., Fabian, A. C., Hatch, N. A., et al. 2008, MNRAS, 386, L72
Flower, D. R., & Pineau des Forêts, G. 1998, MNRAS, 297, 1182
Flower, D. R., Pineau des Forêts, G., & Hartquist, T. W. 1986, MNRAS, 218, 729
Franco, G. A. P. 1989, A&A, 223, 313
Gillmon, K., Shull, J. M., Tumlinson, J., & Danforth, C. 2006, ApJ, 636, 891
Godard, B., Falgarone, E., & Pineau des Forêts, G. 2009, A&A, 495, 847
Goldsmith, P. F., Velusamy, T., Li, D., & Langer, W. D. 2010, ApJ, 715, 1370
Gredel, R., Pineau des Forêts, G., & Federman, S. R. 2002, A&A, 389, 993
Gry, C., Boulanger, F., Nehmé, C., et al. 2002, A&A, 391, 675
Habing, H. J. 1968, Bull. Astron. Inst. Netherlands, 19, 421
Heiles, C., & Troland, T. H. 2003, ApJ, 586, 1067
Hollenbach, D. J., Takahashi, T., & Tielens, A. G. G. M. 1991, ApJ, 377, 192
Houck, J., Roellig, T. L., van Cleve, J., et al. 2004, ApJS, 154, 18
Ingalls, J. G., Reach, W. T., & Bania, T. M. 2002, ApJ, 579, 289
Isobe, T., Feigelson, E. D., Akritas, M. G., & Babu, G. J. 1990, ApJ, 364, 104
Jenkins, E. B., & Tripp, T. M. 2011, ApJ, 734, 65
Jensen, A. G., Snow, T. P., Sonneborn, G., & Rachford, B. L. 2010, ApJ, 711, 1236
Joulain, K., Falgarone, E., Pineau des Forêts, G., & Flower, D. 1998, A&A, 340, 241
Juvela, M., Padoan, P., & Jimenez, R. 2003, ApJ, 591, 258
Kalberla, P. M. W., McClure-Griffiths, N. M., Pisano, D. J., et al. 2010, A&A, 521, 17
Kennicutt, R. C., Jr., Armus, L., Bendo, G., et al. 2003, PASP, 115, 928
Laine, S., Appleton, P. N., Gottesman, S. T., Ashby, M. L. N., & Garland, C. A. 2010, AJ, 140, 753
Lallement, R., Welsh, B. Y., Vergely, J. L., Crifo, F., & Sfeir, D. 2003, A&A, 411, 447
Laureijs, R. J., Fukui, Y., Helou, G., et al. 1995, ApJS, 101, 87
Liszt, H. S., Pety, J., & Lucas, R. 2010, A&A, 518, L45
Magnani, L., Finkbeiner, D. P., Hearty, T., Ingalls, J. G., & Reach, W. T. 2006, , *Spitzer* Proposal ID 30382
Mattila, K., Juvela, M., & Lehtinen, K. 2007, ApJ, 654, L131
Menten, K. M., Wyrowski, F., Belloche, A., et al. 2011, A&A, 525, 77
Meyer, D. M., Lauroesch, J. T., Sofia, U. J., Draine, B. T., & Bertoldi, F. 2001, ApJ, 553, L59
Miville-Deschênes, M. -A., & Lagache, G. 2005, ApJS, 157, 302
Mizuno, A., Yamaguchi, R., Tachihara, K., et al. 2001, PASJ, 53, 1071
Nehmé, C., Gry, C., Boulanger, F., et al. 2008a, A&A, 483, 471
Nehmé, C., Le Bourlot, J., Boulanger, F., Pineau des Forêts, G., & Gry, C. 2008b, A&A, 483, 485
Polk, K. S., Knapp, G. R., Stark, A. A., & Wilson, R. W. 1988, ApJ, 332, 432
Rachford, B. L., Snow, T. P., Destree, J. D., et al. 2009, ApJS, 180, 125
Rachford, B. L., Snow, T. P., Tumlinson, J., et al. 2001, ApJ, 555, 839
Rachford, B. L., Snow, T. P., Tumlinson, J., et al. 2002, ApJ, 577, 221
Roussel, H., Helou, G., Hollenbach, D. J., et al. 2007, ApJ, 669, 959
Shull, J. M., & Hollenbach, D. J. 1978, ApJ, 220, 525
Smith, J. D. T., Draine, B. T., Dale, D. A., et al. 2007, ApJ, 656, 770
Spitzer, L. 1949, ApJ, 109, 337
Spitzer Science Center (SSC) 2009, IRS Instrument Handbook v1.0 (Pasadena, CA: SSC), 6, http://ssc.spitzer.caltech.edu/irs/irsinstrumenthandbook/
Spitzer Science Center (SSC) 2010a, IRAC Instrument Handbook v1.0 (Pasadena, CA: SSC), 41 http://ssc.spitzer.caltech.edu/irac/iracinstrument handbook/
Spitzer Science Center (SSC) 2010b, MIPS Instrument Handbook v2.0 (Pasadena, CA: SSC), 99 http://ssc.spitzer.caltech.edu/mips/mipsinstrument handbook/
Stacey, G. J., Charmandaris, V., Boulanger, F., et al. 2010, ApJ, 721, 59
Tóth, L. V., Haikala, L. K., Liljeström, T., & Mattila, K. 1995, A&A, 295, 755
Wakker, B. P. 2006, ApJS, 163, 282
Welsh, B. Y., Lallement, R., Vergely, J.-L., & Raimont, S. 2010, A&A, 510, 54
Werner, M. 2004, ApJS, 154, 1
Witt, A. N., Gold, B., Barnes, F. S., III, et al. 2010, ApJ, 724, 1551
Wolfire, M. G., McKee, C. F., Hollenbach, D., & Tielens, A. G. G. M. 2003, ApJ, 587, 278